On the breaking of internal solitary waves at a ridge

By J. KRISTIAN SVEEN[1], YAKUN GUO[2],
PETER A. DAVIES[2] AND JOHN GRUE[1]

[1]Mechanics Division, Department of Mathematics, University of Oslo, Blindern, Norway
[2]Department of Civil Engineering, University of Dundee, Dundee DD1 4HN, UK

An experimental laboratory study has been carried out to investigate the propagation of an internal solitary wave of depression and its distortion by a bottom ridge in a two-layer stratified fluid system. Wave profiles, density fields and velocity fields have been measured at three reference locations, namely upstream, downstream and over the ridge. Experiments have been performed with wave amplitudes in the range 0.2–1.9 times the depth of the upper layer, and a ratio between the lower and the upper layer in the range 3.0–8.5. The ridge slope was varied from 0.1 to 0.33 and the maximum ridge height was two-thirds of the thicker fluid layer. Over the ridge, the flow has been classified into: (i) cases when the bottom ridge has little influence on the propagation and spatial structure of the internal solitary wave, (ii) cases where the internal solitary wave is significantly distorted by the blocking effect of the ridge (though no wave breaking occurs), and (iii) cases for which the internal solitary wave is broken as it encounters and passes over the bottom ridge. A detailed description of the processes leading to wave breaking is given. Breaking has been found to take place when the fluid velocity in the lower layer exceeds 0.7 of a local nonlinear wave speed, defined at the top of the ridge. The breaking condition is also expressed in terms of the amplitude of the incident wave, the layer thickness ratio and the relative height of the ridge. The wave breaking can be determined from the input parameters of the experiment. The transmitted waves have been found to always consist of a leading pulse (solitary wave) followed by a dispersive wavetrain. The (solitary) wave amplitude is significantly reduced only when breaking takes place at the ridge. Internal waves of mode two are generated in cases with strong breaking.

1. Introduction

Internal solitary waves that propagate along a density interface have been observed at many locations in the stratified oceans (see, for example, the review articles of Ostrovsky & Stepanyants 1989; Huthnance 1989), with the amplitudes of such waves occasionally exceeding several tens of metres (Osborne, Burch & Scarlet 1978; Osborne & Burch 1980; Sandstrom & Elliott 1984; Apel *et al.* 1985). As internal solitary waves propagate in the ocean, they carry considerable momentum and energy, resulting in significant transient hydrodynamic loading on any offshore structures, undersea navigation vehicles and subsurface storage facilities that they may encounter. At a given location, the passage of the waves results in vertical displacement of the thermocline, with the possibility of significant vertical exchange of fluid and materials as a result of wave-induced mixing.

Owing to their practical importance and theoretical interest, internal solitary waves propagating in a fluid of constant depth have been studied extensively over the past decades, both theoretically (Keulegan 1953; Long 1956; Benjamin 1966; Grue *et al.* 1997; Grue & Ostrovsky 2001) and experimentally (Koop & Butler 1981; Segur & Hammack 1982; Kao, Pan & Renouard 1985; Michallet & Barthelémy 1998). The experimental studies show that Korteweg–de Vries (KdV) theory provides a valid description of solitary waves with small amplitude; more recently, Grue *et al.* (1999) have modelled large-amplitude internal solitary waves in constant depth fluids by means of fully nonlinear theory and have obtained good agreement with their laboratory experiments.

Internal solitary waves moving over one-dimensional topography have been subject to several investigations. Split-up of a single solitary wave in deep water into a number of solitary waves at a shelf was investigated by means of the variable coefficient KdV equation (Ono 1972; Johnson 1973). A disintegration of an incoming solitary wave into a dispersive wave packet was noted by Djordjevic & Redekopp (1978). The process of disintegration of an initial solitary wave of depression after the turning point, i.e. the point where the pycnocline is half-way between the seabed and the sea surface, and the appearance of new solitary waves of elevation, was further pursued by Knickerbocker & Newell (1980), Helfrich, Melville & Miles (1984) and Malomed & Shrira (1991). Grimshaw, Pelinovsky & Talipova (1998) gave a detailed numerical study of the solitary wave transformation at a slope and change of polarity. In the case of a short transition zone, they found no solitary wave after passage through the turning point. If the transition was slow, however, their simulations showed that new solitary waves were generated by the deformation of the leading wave and by a wave of elevation appearing behind the solitary wave.

Fission of a barotropic or a baroclinic solitary wave incident on a step-like topography, was studied by Kabbaj (1985) and Renouard, Seabra Santros & Zhang (1987), whereas Kabbaj & Zhang (1988) described the fission of an internal solitary wave passing over a sill, comparing the Djordjevic & Redekopp model and the Kabbaj model. Whereas the former gave information only of the transmitted wave, the latter also included a reflected wave. Transmission and reflection of internal solitary waves of depression at a topography (thin layer above thick layer, and topography in the thick layer) were studied further by Diebels, Schuster & Hutter (1994) and Wessels & Hutter (1996). (Similar reflection and transmission are observed in our experiments, although this is not the main focus here.) In the sets of experiments with a solitary wave of elevation interacting with a bottom ridge (thick layer above thin), a pronounced reflection wave was measured when the height of the topography exceeded the thickness of the thin layer. A study of transmission and reflection of solitary surface waves by a semicircular cylindrical obstacle in a one-layer fluid was performed by Cooker *et al.* (1990).

Experiments on the shoaling processes of an internal solitary wave over a uniform sloping bottom were carried out by Kao *et al.* (1985), who observed that sufficiently high waves were able to break on a slope. Helfrich (1992) measured the conversion of solitary waves into boluses. Michallet & Ivey (1999) examined the mixing process and quantified the energy loss associated with internal solitary waves breaking over a uniformly sloping bottom.

The main objective of the present study is the process of internal wave breaking at a ridge. The velocity and density field perturbations associated with the passage of an internal solitary wave over a bottom ridge are measured. The flow regimes associated with the ridge encounter are classified. A general breaking criterion is
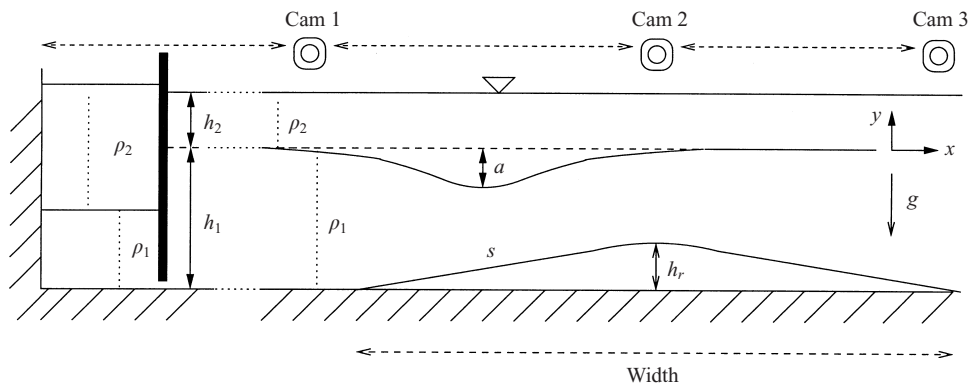
FIGURE 1. Sketch of the experimental arrangement with Cam 1, Cam 2 and Cam 3 denoting the positions of the cameras.

justified. Experiments are performed for wave amplitudes ranging from 0.2 to 1.9 times the upper layer thickness, and depth-ratios in the range 3.0 to 8.5. The ridge slope is varied from 0.1 to 0.33 and the maximum ridge height is two-thirds of the thicker fluid layer.

The sections of the paper include: the experimental arrangement (§ 2), the experimental and theoretical description of the incoming solitary waves (§ 3), description of the wave–ridge encounter and the wave breaking (§ 4), and wave transimission and reflection (§§ 5 and 6). Conclusions are given in § 7.

2. Experimental arrangement

Figure 1 shows a schematic diagram of the wave tank and measurement positions. An internal solitary wave of amplitude a is generated in a stably stratified fluid system of total depth $h_1 + h_2$ and comprising lower (subscript 1) and upper (subscript 2) layers of thickness $h_{1,2}$ and density $\rho_{1,2}$. The propagating wave moves with speed c and amplitude a, and passes over a two-dimensional ridge of maximum height h_r and side slope s attached to the horizontal bottom surface of the system.

The behaviour of the incoming wave may be characterized in terms of h_1/h_2, a/h_2 and c_0, where the latter denotes the linear long-wave speed given by (in the Boussinesq limit)

$$c_0 = \sqrt{\frac{g'h_1h_2}{h_1 + h_2}}, \tag{2.1}$$

where $g' = g(\rho_1 - \rho_2)/\rho_1$ and g is the acceleration due to gravity (Grue *et al.* 1999).

The experiments were conducted in two different channels having overall dimensions of 25.0 m×0.5 m×1.0 m and 6.4 m×0.4 m×0.6 m (length, width and depth, respectively). In the long wave tank, experiments were performed in two different sections of either 15.3 m or 21.5 m length. Experiments were performed with a two-layer fluid with a lower homogeneous layer of brine and a layer of fresh water slowly added on top of the lower layer through a floating sponge arrangement. For practical reasons, the values of ρ_1 and ρ_2 may vary somewhat from their prescribed values from run to run. This does not influence the results as long as the linear long-wave speed, c_0, determined by (2.1), is used as the reference speed.

Wave tank	Ridge width (m)	Ridge height (m)	Slope
Small	0.6	0.1	0.33
Small	1.0	0.1	0.20
Small	0.9	0.15	0.33
Large	6.2	0.31	0.10

TABLE 1. Different ridges used in the experiments.

Tank	Cam 1 (m)	Cam 2 (m)	Cam 3 (m)	Tank width (m)	Tank length (m)	ρ_1 g cm^{-3}	ρ_2 g cm^{-3}
Large	4.5	7.5	12.1	0.5	15.3, 21.5	1.022...	0.998...
Small	3.2	4.05	4.9	0.4	6.4	1.045–1.052	1.029–1.033

TABLE 2. Table of measurement positions.

2.1. *Ridge*

Experiments were performed both with and without a bottom ridge present in the channel. A total of four different ridges were used and they were constructed out of transparent plastic, but masked allow light to come through in the form of a light sheet. The ridges were designed and machined with straight sides joined by an arc in such a way that the slope sides aligned smoothly with the end points of the arc.

The ridge was carefully positioned at a distance sufficiently far from the gate that the waves were steady before encountering it. In the small channel, the centre of the ridge was positioned at a distance of 4.05 m from the endwall of the tank where the wave was generated. In the large channel, the highest point of the ridge was positioned at a distance of 7.83 m from the corresponding endwall. The ridges had varying heights in the range from 0.1 m to 0.31 m with slopes from 0.1 to 0.33 (see table 1).

2.2. *Measurement positions*

In all the experiments, measurements were performed at three different positions in the wave tank. The first was used to document the incoming wave, the second monitored the encounter with the ridge, while the third monitored the waves transmitted from the ridge. The cameras were placed at the positions described in table 2, and all the distances were measured from the endwall of the channel where the waves were generated.

2.3. *Wave generation*

The wave generation mechanism follows the method described by, e.g. Grue *et al.* (1999) and Kao *et al.* (1985). A movable gate was installed at one end of the channel after the two-layer system was configured. Behind this gate a volume of water of density ρ_2 could be trapped. Hydrostatic balance was maintained by leaving open a small gap beneath the gate. Upon release of the gate an internal wave was generated, propagating along the interface in the initially undisturbed working section. By carefully adjusting the position of the gate and the initial volume behind it, a single solitary wave of prescribed amplitude a (see Grue *et al.* 1999) could be generated (see figure 1). Experiments were performed covering a large range of model parameters (see table 4). Table 3 lists 16 experiments selected out of a total of 56 performed.

Experiment number	Tank	h_1	h_2	a/h_2	h_r	h_l	c_0
swl2	1	0.45	0.15	0.55	0.305	6.1	0.1589
swl3	1	0.45	0.15	0.10	0.305	6.1	0.1609
swl4	1	0.45	0.15	0.40	0.305	6.1	0.1619
swl5	1	0.45	0.15	0.34	0.305	6.1	0.1609
swl6	1	0.54	0.15	0.64	0.305	6.1	0.1596
swl7	1	0.45	0.14	0.25	0.305	6.1	0.1542
swl8	1	0.45	0.10	0.59	0.305	6.1	0.1372
swl9	1	0.54	0.10	0.79	0.305	6.1	0.1388
swl10	1	0.54	0.10	0.38	0.305	6.1	0.1382
se10	2	0.241	0.059	1.03	0.10	1.0	0.0746
se45	2	0.305	0.075	0.79	0.15	0.932	0.0840
se47	2	0.241	0.059	0.96	0.15	0.932	0.0746
se48	2	0.241	0.059	0.54	0.15	0.932	0.0976
se49	2	0.241	0.059	0.96	0.15	0.932	0.0975
sw31	2	0.241	0.059	1.01	0.10	0.6	0.0746
sw32	2	0.2685	0.0315	1.81	0.10	0.6	0.0752

TABLE 3. Selected experiments performed in the large tank (1) and the small tank (2).

$\Delta\rho/\rho_1$	h_1/h_2	$h_1 + h_2$ (cm)	a/h_2
0.0119–0.0237	3–8.5	30–77	0.2–1.9

TABLE 4. Ranges of parameters used in the experiments.

2.4. *Particle tracking and particle image velocimetry*

Particle tracking velocimetry (PTV) and particle image velocimetry (PIV) represent powerful non-intrusive measurement techniques to quantify the velocities and the underlying dynamics in a two-dimensional slice of the flow in the wave tank. In the present study, both methods were applied to measure velocities.

In the PTV method, individual particles are traced in sequences of images. This method is ideal when the local fluid acceleration is relatively small (which is true when the wave amplitude is small or moderate and there is no or little interaction between the wave and the ridge). In the PIV method, the spatial cross-correlation between the position of groups of particles at two subsequent time instants is evaluated to estimate the local fluid velocity. The motion due to the moderate waves was analysed here using both PTV and PIV. For the cases where wave breaking occurred, it was found that PIV was required for more precise measurements of the fluid motion.

Recordings were made in vertical sections of the wave tank by three monochrome COHU 4912 CCD cameras with a resolution of 575×560 pixels. In the large tank, light sheets were generated by the use of powerful overhead projectors, while in the small tank, light sheets were generated by the use of powerful arc lamps. The light sheets were vertical and parallel to the side of the tank.

In the large tank, the illuminated sections were seeded with particles of Pliolite VTAC with diameters in the range of 0.8–1 mm. The particles were treated in wetting agent for some time to obtain an effective neutral buoyancy for the range of the density profile. In the small tank, acrylic particles of type *Optimage* were used, having a nominal diameter of 0.25 mm.

The video recordings were digitized by a frame grabber card for subsequent analysis. Typically 600–2000 particles were identified in each frame. In the PTV method, particles were traced during five frames (equals to 0.2 s) using the DigImage program developed and described by Dalziel (1992, 1993).

For PIV analysis, the software program MatPIV v1.4 (Sveen 1998) was used, as developed in house. The code is an implementation of the method outlined in Willert & Gharib (1991), but additionally employs interrogation window shifting as proposed by Westerweel, Dabiri & Gharib (1997). The images were interrogated in three steps where the first step was used to estimate the window shift with integer accuracy using twice the desired interrogation window size. Subsequently, the interrogation regions were halved before the second pass where the displacements were still measured with integer accuracy using the estimates from the first pass as a guide. The third and final pass then used the estimated displacements to shift the interrogation regions in the second image. The displacements were found to subpixel accuracy using a standard, three-point Gaussian fit of the correlation peak. Images were interrogated using interrogation windows of 32×32 pixels. The final velocity vectors were validated using a signal to noise ratio filter, where the signal to noise ratio was determined by the highest peak in the correlation plane divided by the second highest peak. Normally, it was required that this ratio be larger than 1.15, and vectors not satisfying this threshold were rejected. Subsequently, a global filter was applied to remove vectors that were larger than 3 times the standard deviation of all the vectors, followed by a local median filter to effectively remove vectors that are larger than 1.7 times the median value of the neighbouring points of a vector. Finally, erroneous vectors were replaced using a nearest neighbour interpolation.

2.5. *Density measurements*

To monitor the density profiles before the experiments in the large tank, a conductivity meter (Yokogawa SC12) was used. These measurements were complemented by the use of a very accurate density meter (Mettler-Toledo DA-300M) which determines the density with an accuracy of five significant digits. In the small tank, a computer-controlled array of traversing, fast response microconductivity probes (see Head 1983) was deployed. This array of probes was also used during wave propagation to capture quasi-instantaneous vertical density profiles at different locations in the tank.

2.6. *Interface tracking from PIV images*

Each experiment usually resulted in the acquisition of video recordings at the three different camera positions. At each position, a time sequence of images was then available for PTV and PIV measurements. In these experiments, the tracer particles used tend to coalesce in the interface region. This means that this area in the images will have a higher mean intensity than the rest of the image. Here, a novel technique is described to track this intensity in the images. The technique is applied to the measurements of the transmitted wave at the third camera position in the long-wave tank.

Typically, these recordings were more than 2 min long and images 0.52 s apart are grabbed. From each image, A, 21 columns of data are extracted from the centre area ($A(246 < i < 266, j = 1$–$512)$). Then a row-wise mean is performed so that a single column of data representing the average image intensity in the centre area is generated. This operation is performed on all the images available in the sequence and the final result is a time trace of the wave as it passes the camera. Following this, a polynomial filter is applied to smooth high-frequency noise and a

one-dimensional cross-correlation of the individual columns of data is performed to find the displacement of the intensity peak associated with the interface. This means that each column in A is cross-correlated with its first column. The peak in each correlation signal (one for each column) is then located together with the position of the maximum gradient on both sides of the peak. The maximum gradient is used as an indicator of the thickness of the high-intensity area which again relates to the thickness of the interface in the experiments. In this way, the motion of the interface can be monitored accurately. In the same manner as in ordinary PIV, the result is then converted to so-called world-coordinates using a linear mapping function.

It is noted that the position of the maximum gradient of the correlation peak does not necessarily give a direct measure of the thickness of the pycnocline. Rather it gives a measure of both the accuracy with which the correlation peak can be determined, and the vertical spread of particles close to or at the pycnocline. A more thorough investigation of this method is needed, but is beyond the scope of this paper.

2.7. *Experimental accuracy*

The accuracy of the PTV method applied to internal wave experiments in a two-layer fluid, with a constant density in each layer, has been analysed in earlier works (see Grue *et al.* 1999, §§ 2.3 and 7) where it was found that the error in the measured velocities relative to the linear long-wave speed was less than about 7–8% in all cases. This analysis is also valid for the present experiments.

Comparison between the PTV and PIV measurements shows that the accuracy of the two methods in practical aspects is approximately the same for the present experiments. A more detailed analysis of the accuracy in PIV experiments may be found in Raffel, Willert & Kompenhans (1998). This level of accuracy also applies to the method for finding the interface, as it is based on the use of the cross-correlation function.

3. The incident wave

The incoming waves were measured at the first camera position located 3.2 m from the gate. Figure 2 shows measured horizontal velocity profiles for a few selected experiments for non-dimensional amplitudes $a/h_2 = 0.25$, 0.58 and 1.08 and corresponding depth ratios $h_1/h_2 = 3.21$, 3.0 and 4.5. The profiles were measured at the trough of the waves and comparison was made with the fully nonlinear theory of Grue *et al.* (1999). For all three cases, a good correspondence was observed between the measurements and the theory. All of the profiles were seen to have a weak dependence on the vertical coordinate in each layer.

When internal waves are generated in the laboratory, it is important to consider the influence of the different parameters involved. In the present cases where wave tanks with different fluid depths have been used, the relative thickness of the interface, δ, between the two fluids may play a more important role in reconciling results from each geometry. In both tanks, this interface thickness will be of similar size owing to the mechanism used to fill the tank. The quantity, δ, therefore played a more influential role in the small tank where the layer thicknesses were smaller. Accordingly, in order to distinguish between the experiments performed in the large and the small wave tanks, the relative interface thickness, δ/h_2 has been adopted as a comparison parameter. Figures 3(a) and 3(c) show measurements of the horizontal velocity component, u_2, measured in the middle of the upper layer, at $y = \frac{1}{2}h_2$, and normalized by c_0 with the latter given in (2.1). Figures 3(b) and 3(d) show the corresponding measurements in
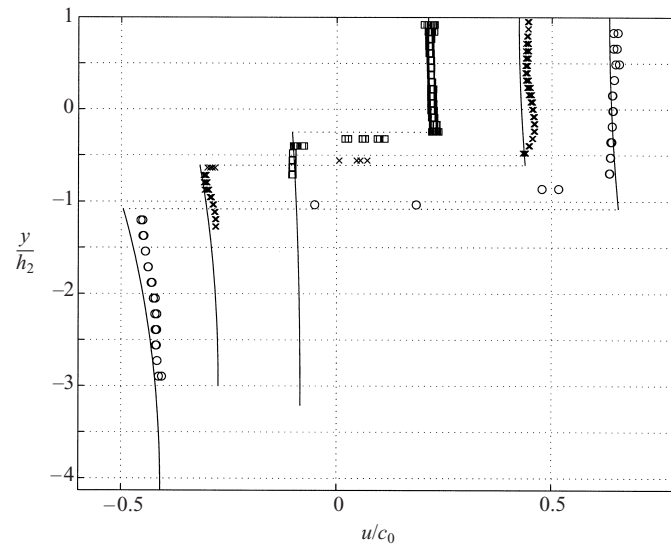
FIGURE 2. Non-dimensional horizontal velocity at wave trough *vs.* non-dimensional depth. $\square$, $a/h_2 = 0.25$, $h_1/h_2 = 3.21$; $\times$, $a/h_2 = 0.58$, $h_1/h_2 = 3.0$; $\bigcirc$, $a/h_2 = 1.08$, $h_1/h_2 = 4.5$. Solid lines were results from fully nonlinear theory.
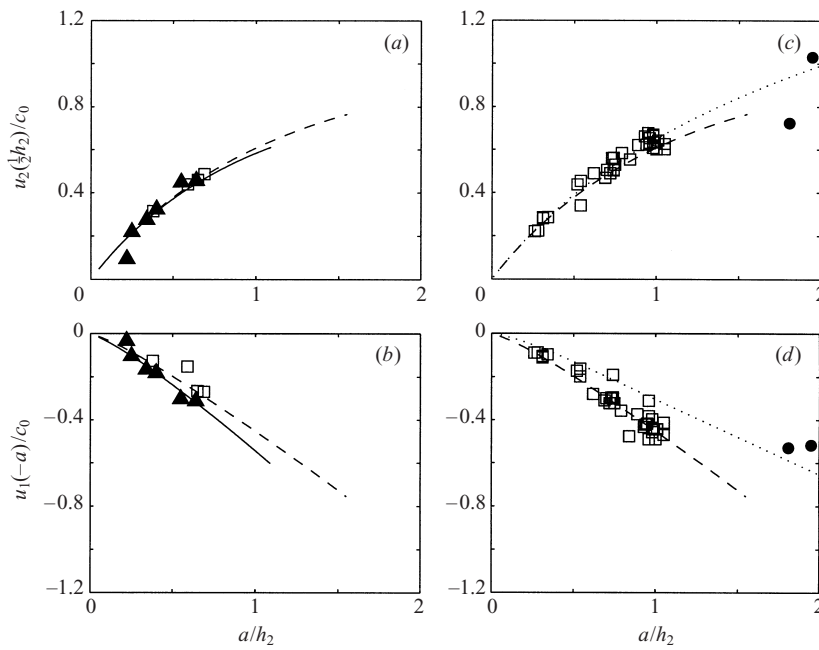

FIGURE 3. Non-dimensional horizontal velocity at wave trough *vs.* non-dimensional amplitude a/h_2. (*a*, *b*) Experiments in the large wave tank, (*c*, *d*) small tank. (*a*, *c*) Velocity in the upper layer, $u_2(y = h_2/2)$. (*b*, *d*) Velocity in the lower layer, $u_1(y = -a)$. $\blacktriangle$, Experiments where $h_1/h_2 = 3.0$–3.6; ——, fully nonlinear theory for $h_1/h_2 = 3.2$. $\square$, Experiments with $h_1/h_2 = 4.1$–5.4; – – –, theory using $h_1/h_2 = 4.13$. $\bullet$, Experiments where $h_1/h_2 = 8.5$; $\cdots\cdots$, the corresponding theory.

the lower layer measured at the maximum displacement of the pycnocline, at $y = -a$. The figures show all of the experiments contained in this paper and demonstrate the accuracy in our measurements.

Figures 3(a) and 3(b) show plots of all the experiments performed in the long wave tank. In this case the relative thickness of the pycnocline is estimated to be $\delta/h_2 \sim$ 0.13–0.2. In the small channel this relative thickness is typically $\delta/h_2 \sim$ 0.27–0.34 and amplitude estimates are somewhat less precise than for a thin pycnocline.

In general, a good agreement between the theory and the experiments is found although some scatter in the data is present. The scatter appears to be slightly larger for the experiments performed in the small channel and this finding is attributed mainly to the fact that the relative thickness of the interface is larger in this case.

3.1. *Wave profiles*

To test the influence of the ridge on the upstream wave, two experiments were performed in the small tank with identical initial conditions. The first experiment was performed with a ridge present and the second without. The results for two waves from two separate experiments with $a/h_2 = 0.31$ (not shown here), confirm that the difference between the two measured wave profiles is negligible at the first camera position. Furthermore, the agreement with the theoretical prediction of a steady wave is very good, apart from a small transient tail in the experiment.

4. The wave–ridge encounter

4.1. *Weak and moderate wave–ridge encounters*

The second camera monitors the encounter of waves with the bottom topography. The camera was in all cases positioned so that the top of the ridge was within or directly below the field of view. Experiments were performed for a wide range of parameters, covering cases from practically no interaction to cases with strong breaking. The waves are in all cases moving from left to right in the pictures.

When the amplitude of the incoming wave is sufficiently small compared with the height of the ridge, the interaction is weak, as shown in figure 4(a). As the wave passes the ridge, the velocity in the lower layer is increased owing to the decreased local depth, but there is no breaking taking place and the wave shape is not significantly distorted.

As the relative blocking effect exerted by the ridge is increased, the deformation of the wave changes from weak to moderate (figure 4b). The velocity in the lower layer is increased significantly as a result of the decreased local water depth. Separation is observed to take place at the ridge but no significant three-dimensional motion is observed after the encounter. The separation leads, in most cases, to the generation of one or more vortices that propagate along the bottom and eventually dissipate near the top of the ridge (details are given in §4.4). Figure 5 shows the density profile measured directly above the ridge before and during the passing of a wave in an experiment where no breaking is observed (experiment *se10*, see table 3). The thickness of the interface is increased, but no mixing or overturning takes place, as the wave passes the ridge.

4.2. *The breaking events*

4.2.1. *Wide ridge*

As the wave–ridge encounter increases in strength, wave breaking is observed (figures 4c, 6 and 7). Wave breaking at the wide ridge is discussed first. Figure 6
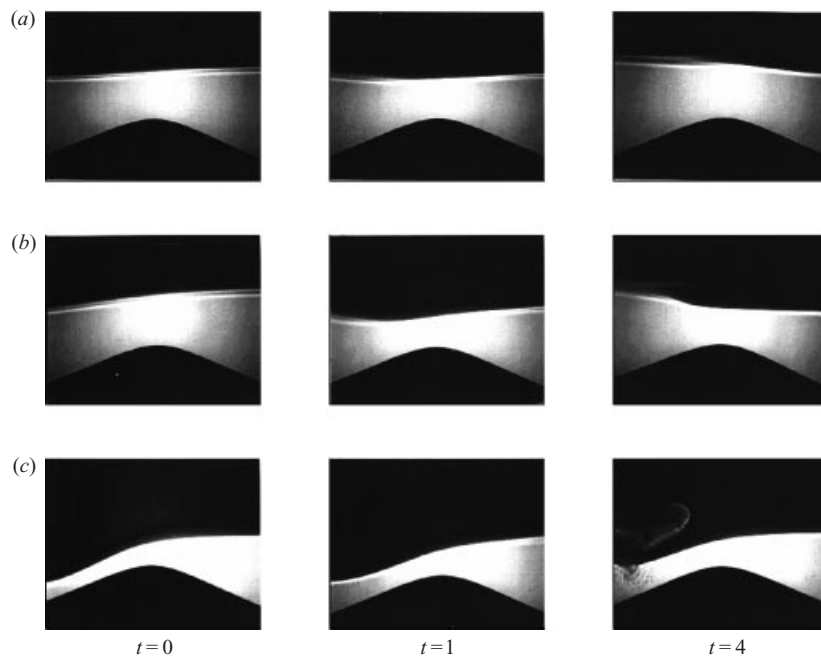
FIGURE 4. Time sequences of shadowgraph showing (a) weak encounter ($a/h_2 = 0.3$); (b) moderate encounter in which the wave is distorted significantly, though no breaking ($a/h_2 = 0.42$) and (c) strong encounter with wave breaking ($a/h_2 = 0.98$). In all cases, $h_1/h_2 = 4.1$, $h_r/h_2 = 2.54$ (short tank).

illustrates the breaking process with six images taken at time $t = t_0$, $t_0 + 5$ s, $t_0 + 6.96$ s, $t_0 + 7.96$ s, $t_0 + 10$ s and $t_0 + 14$ s. In figure 6(a) the interface is observed to be aligned almost parallel to the side slope of the ridge. In the frame in figure 6(b), taken 5 s later, the rear part of the wave has reached the field of view and the steepest part of the interface (for $-2.5 < x/h_2 < -1.5$) is almost perpendicular to the slope of the ridge. It is observed that the interface extends deeper than half of the local water column. The incident depression wave is transferred into a leading depression and a subsequent wave of elevation (figure 6b–d). This is similar to the transformation process of interfacial solitary waves of depression travelling up a sloping beach, beyond the turning point (the point where the pycnocline is halfway between the sea bed and the sea surface). This was, in the weakly nonlinear and non-breaking cases, described in Knickerbocker & Newell (1980), Helfrich et al. (1984), Malomed & Shrira (1991) and Grimshaw et al. (1998). The process here is more pronounced than what can be modelled by the long-wave equations, however. In figure 6(b), it can be seen that the interface at the rear of the wave is thicker and that the mixing of salt and fresh water creates a foglike small area at the interface, indicating breaking flows. In figure 6(c) the wave is weakly overturning.

A second breaking event occurs where the tail of the wave has become so steep that the pycnocline collapses locally. The elevation, behind the leading pulse, is then almost at the top of the ridge (figure 6e). Such a breaking behind the wave of elevation is not observed in the weak and moderate wave–ridge encounters. Neither is it observed for a narrow ridge. We cannot exclude the possibility that in this case the local vertical acceleration is comparable to the acceleration due to gravity, g, i.e. a Rayleigh–Taylor instability. Rough acceleration estimates indicate a value of
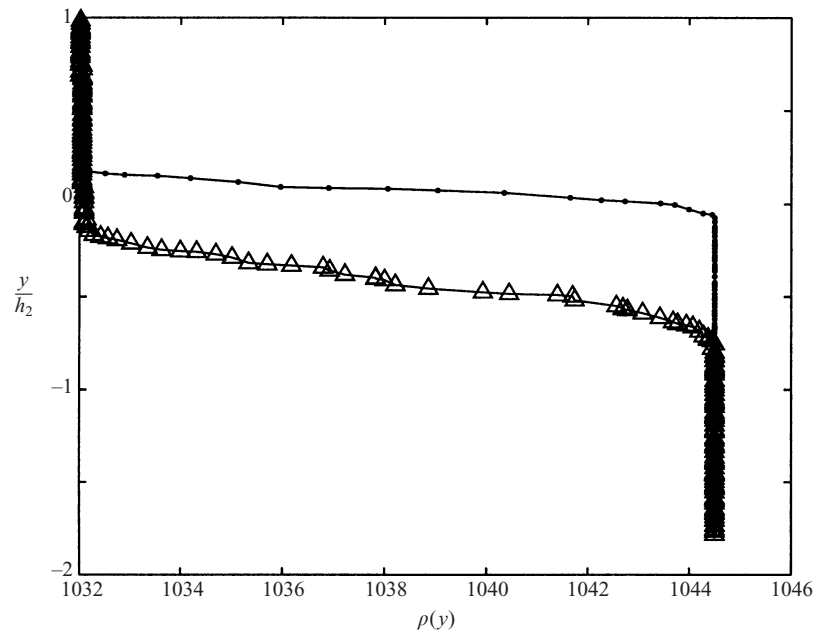
FIGURE 5. Density profile *vs.* non-dimensional depth measured at the initial state and through the wave as the wave passes the ridge. $a/h_2 = 1.033$, $h_1/h_2 = 4.1$, $h_r/h_2 = 1.69$ for the short tank. The dot-connected line shows the initial density profile, whereas the triangle-connected line shows the profile near the maximum excursion of the interface as the wave is passing the ridge. The wave is distorted by the ridge but no breaking is observed.

about $0.5\,g$, however. The elevation behind the leading pulse can also be explained by a transition between the almost critical flow occurring beneath the wave trough, and the flow that is far from critical in the rear part of the wave, with a higher excursion of the pycnocline. A similar behaviour is observed in free surface flows. An example is the interaction between a solitary wave of elevation and a submerged obstacle (Cooker *et al.* 1990, § 3.3). Another example is a thin hydrofoil moving with speed U and submergence h below the free surface in otherwise calm water. A strong interaction between the foil and the free surface takes place when $U/\sqrt{gh}$ is equal to unity (Hough & Moran 1969; Walree 1999).

For increasingly stronger interaction, the local flow above the ridge crest becomes supercritical. The flow forming the wave of elevation then develops into a hydraulic jump. The position of the latter appears earlier and earlier on the slope, for increasing strength of the wave–ridge encounter.

Table 5 summarizes the observations from 10 different experiments, where the 5 first are experiments with a wide ridge and the final 5 with a narrow one.

4.2.2. *Narrow ridges*

In the experiments where the narrower ridges were used, the wave breaking is more rapid and always in the form of overturning. The breaking in the form of a collapse was never observed in these cases. Figure 7 shows four images from the experiment labelled *se49*, where $|\tilde{u}_1|/\tilde{c}_0 \sim 1.19$ ($\tilde{c}_0$ and $\tilde{u}_1$ are defined in § 4.5). Figure 7(*a*) shows the wave just before overturning, as it enters the field of view. In figure 7(*b*), the overturning has started, and in figure 7(*c*) a large plunging jet is seen. Figure 7(*d*) shows the wave 3.6 s after the first image, and now eddies can be seen on the interface
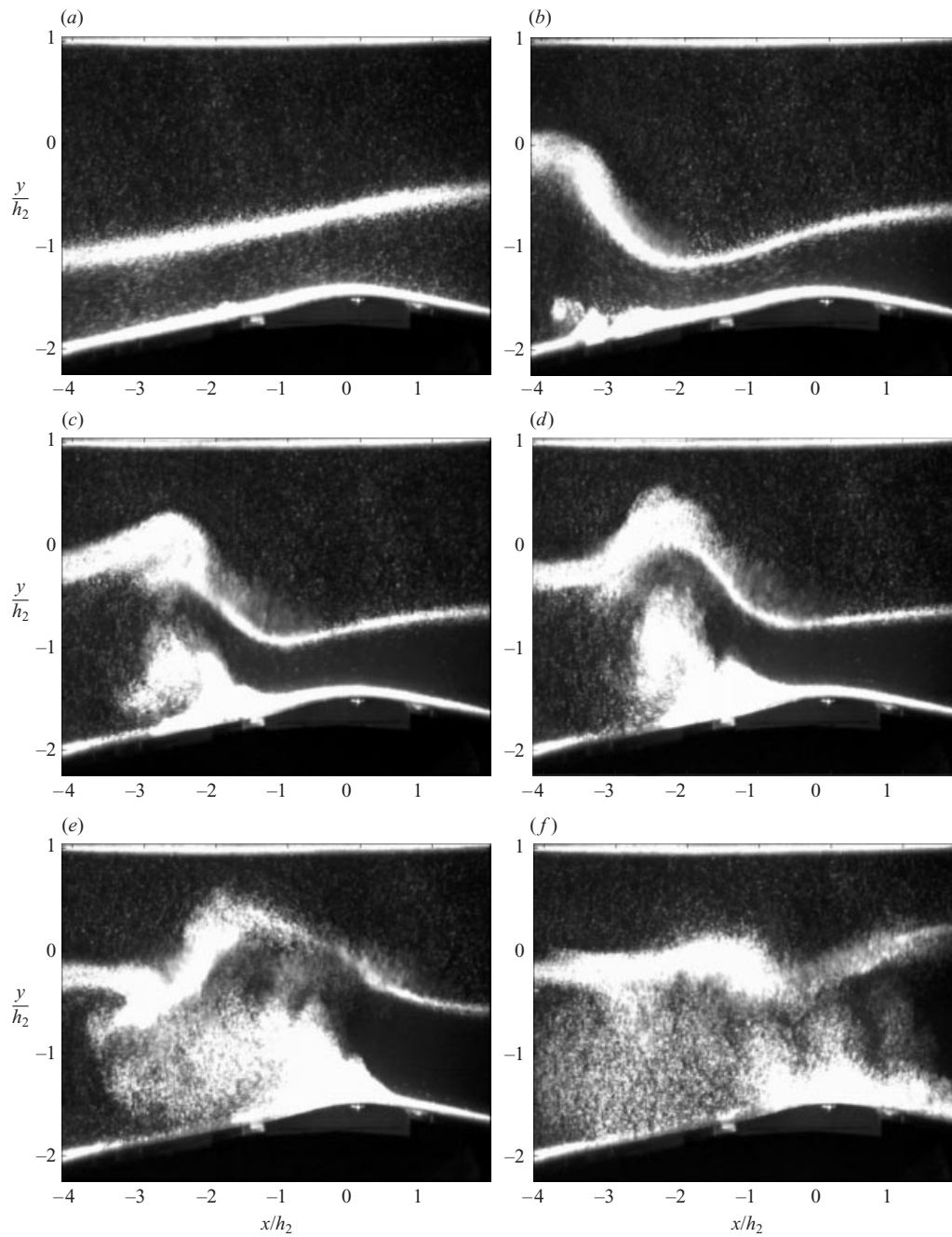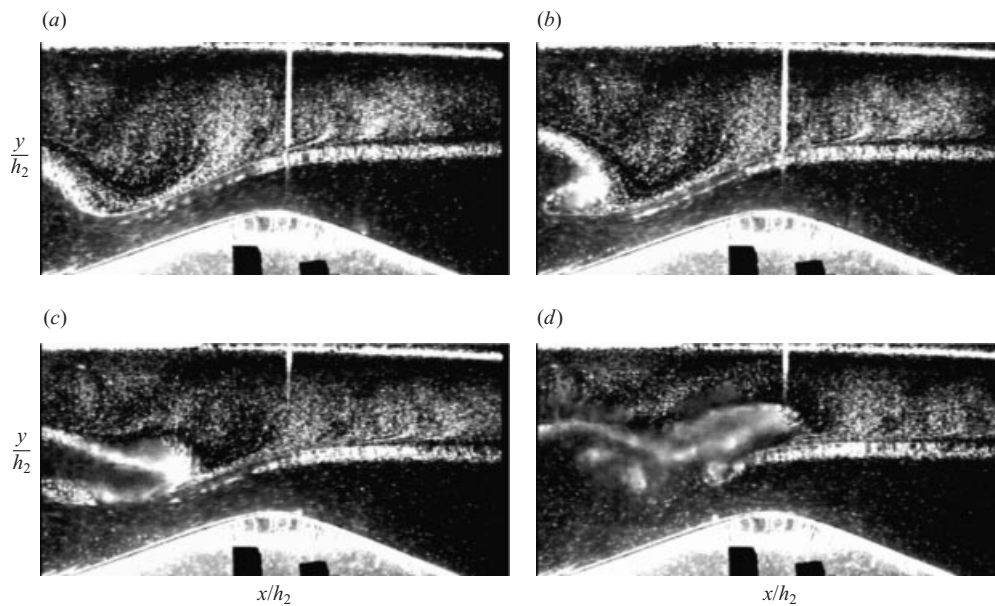
FIGURE 6. Image sequences showing a wave breaking event for the wide ridge. (*a*) $t = t_0$, (*b*) $t = t_0 + 5$ s, (*c*) $t = t_0 + 6.96$ s, (*d*) $t = t_0 + 7.96$ s, (*e*) $t = t_0 + 10$ s and (*f*) $t = t_0 + 14$ s. The images are taken from an experiment performed in the large wave tank with $h_1/h_2 = 4.5$, $h_r/h_2 = 3.1$ and $a/h_2 = 0.59$. Experiment *swl8*.

Exp	$|\tilde{u}_1|/\tilde{c}_0$	$\dfrac{a + h_2}{h_1 + h_2 - h_r}$	Overturning	Collapse at rear	Comment
swl2	1.0	0.79	No	Yes	Spilling breaker, powerful mixing
swl4	0.84	0.71	No	Yes	Weak, spilling breaker
swl5	0.71	0.68	No	No	Weak, spilling breaker
swl6	0.88	0.64	No	Yes	Weak, spilling breaker
swl8	1.15	0.65	Yes	Yes	Strong breaking, powerful mixing
se47	1.49	0.78	Yes	No	Strong breaking
se48	1.0	0.64	Yes	No	Strong breaking
se49	1.19	0.77	Yes	No	Strong breaking
sw31	0.94	0.59	Yes	No	Strong breaking
sw32	0.67	0.44	Yes	No	Weaker breaking

TABLE 5. Table of different observations of breaking. All experiments labelled *swl* . . . are with a wide ridge. $\tilde{c}_0$ defined in equation (4.4).

FIGURE 7. Image sequences showing a wave-breaking event for the narrow ridge. (*a*) $t = t_0$, (*b*) $t = t_0 + 1.2\,\mathrm{s}$, (*c*) $t = t_0 + 2\,\mathrm{s}$, (*d*) $t = t_0 + 3.6\,\mathrm{s}$. The images are taken from an experiment performed in the short wave tank with $h_1/h_2 = 4.1$, $h_r/h_2 = 2.54$ and $a/h_2 = 0.96$. Experiment *se49*.

between the jet and the initial interface. Three eddies are identified in the image. The density probe can also be seen as a vertical line at the top and centre of all the images.

4.3. *Measurements of overturning*

In the experiments using the narrow ridges, the wave breaking is dominated by overturning. The degree of overturning may be quantified conveniently by processing the sequential density profile measurements (figure 8, experiment *se49*) in terms of the
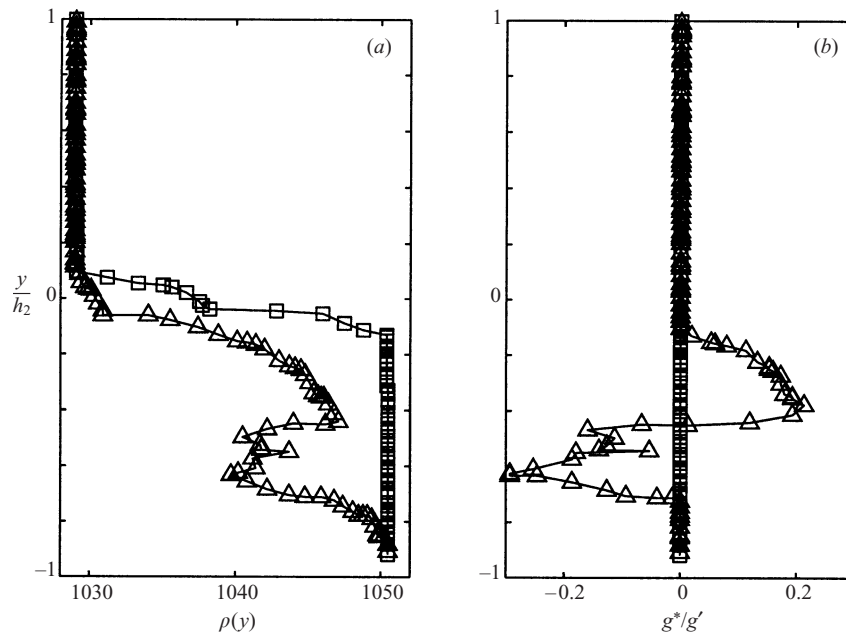
FIGURE 8. Density variations due to breaking measured in the experiment *se49* with $a/h_2 = 0.96$, $h_1/h_2 = 4.1$ and $h_r/h_2 = 2.54$. (*b*) Normalized buoyancy anomaly. Line-connected squares: initial density profile. Line-connected triangles: Density profile taken during breaking.

instantaneous buoyancy anomaly profile $g^*(y_i)$ defined (De Silva, Imberger & Ivey 1997) here as:

$$g^*(y_i) = \frac{g}{\rho_m}[\rho(y_i) - T(y_i)], \tag{4.1}$$

where $\rho(y_i)$ is the measured instantaneous density profile over the ridge crest, $T(y_i)$ is the corresponding Thorpe-ordered density profile and ρ_m is the mean density. $T(y_i)$ is found by monotonizing $\rho(y_i)$ so that the sequence has minimum potential energy.

The result for one experiment is shown in figure 8(*b*) where the buoyancy anomaly g^* is normalized by $g' = g\Delta\rho/\rho$ (initially unperturbed reduced gravitational acceleration). The initial profile is seen to have a buoyancy anomaly of zero. For the instantaneous profile measured at the wave crest, the variations visible in figure 8(*a*) give rise to a buoyancy anomaly $-0.25 < g^*/g' < 0.2$, indicating the amount of overturning present. The vertical extent of the overturning region in this case is estimated to be about $0.6h_2$. For weak wave-breaking cases, mixing and overturning events are also observed to take place, though, as expected, the events are not as vigorous as those observed in strong wave-breaking cases and the values of g^*/g' are correspondingly lower.

4.4. *Generation of vortices*

Vortices were observed to be generated at the weather side of the ridge as a wave propagated over it for all events where moderate or strong interaction occurred, but the position at which the vortices were produced and their development varied as the relative amplitude increased. Depending on the velocities induced by the wave, there may be more than one vortex generated owing to the flow separation.

The vortices are generated as a consequence of flow separation owing to an adverse

pressure gradient on the ridge bed as the wave tail rises steeply. The separation starts with a surge-like flow upwards along the bottom and develops into a flow containing one or more vortices. Particles located on the bottom topography are observed to be swept off and mixed into the entire column of the lower layer.

In the cases where moderate interaction was observed between the wave and the ridge, the vortex or vortices generated moved up along the ridge crest and eventually dissipated near the top of the ridge. In the experiment labelled *swl9* (see table 3), two vortices were observed to be generated, each having a diameter of about $d_v \sim 0.5h_2$. The lifespan of these vortices may be estimated to be of the order of $tc_0/a \sim 25$, with a denoting the incoming amplitude and c_0 the linear long-wave speed without the ridge present. The dissipation of these relatively long-lived vortices may be ascribed to the weak viscous effect that attenuates their vorticity.

In the cases where strong breaking was observed, the vortex generation and eventual breakdown was more powerful. Looking to figure 6(*b*), initial separation is seen to be taking place. At $x/h_2 \sim -2.5$, $y/h_2 \sim -1.6$, the image shows a vortex being shed. This vortex eventually moves up along the ridge (see figure 6*d*) and it is paired with a larger one at $x/h_2 \sim -1.5$, $y/h_2 \sim -1$. This larger vortex is created at a later time than the first and at a position further up the ridge slope. Looking to figure 6(*e*), the flow which initially separated from the ridge has developed and now extends in a larger region with strong mixing. The motion in this region seems to break down into small-scale motion. Visual observations confirm that the motion in this case is three-dimensional. In this image, the point where the separation begins has moved to the top of the ridge at $x/h_2 \sim 1$.

The two vortices mentioned above, have diameters $d_v \sim 0.2h_2$ and $d_v \sim h_2$, respectively. The smaller of the two was generated first and disappeared after about $tc_0/a \sim 7$ into the larger vortex. The latter had an estimated time span of about $tc_0/a \sim 9$. As the wave eventually breaks, the local flow structure becomes turbulent and leads to breakdown of the vortex. The structure of the vortex is destroyed *in situ* by turbulence approximately where it is generated.

The experiments with breaking have revealed that the subsequent mixing takes place throughout the whole column of the lower layer. In extreme cases, particles have been observed to move across the interface.

4.5. *Quantitative analysis of the wave breaking at camera 2*

To quantify the degree of interaction, the horizontal velocities, $u_1^{\text{cam2}}(x, y, t)$ and $u_2^{\text{cam2}}(x, y, t)$ are measured, in the lower and upper layer, respectively, above the top of the ridge. Subsequently a mean is taken over a small area in both layers by defining

$$u_1^{c2}(t) = \frac{1}{0.04h_2} \int_{h_r}^{h_r+0.2h_2} \int_{x_0-0.1h_2}^{x_0+0.1h_2} u_1^{\text{cam2}}(x, y, t)\, dx\, dy, \qquad (4.2)$$

$$u_2^{c2}(t) = \frac{1}{0.1h_2} \int_{y_0+0.4h_2}^{y_0+0.9h_2} \int_{x_0-0.1h_2}^{x_0+0.1h_2} u_2^{\text{cam2}}(x, y, t)\, dx\, dy, \qquad (4.3)$$

where x_0 denotes the position of the crest of the ridge and y_0 the position of the undisturbed interface. The integration area is restricted owing to uncertain measurements close the free surface and the pycnocline. The results from two different experiments are plotted in figure 9, where the data have been non-dimensionalized by $\tilde{c}_0$ (defined below).

To examine more closely the breaking process, it is convenient to introduce the minimum velocity in the lower layer, $\tilde{u}_1(t = t_0) = \min(u_1^{c2}(t))$ and the maximum

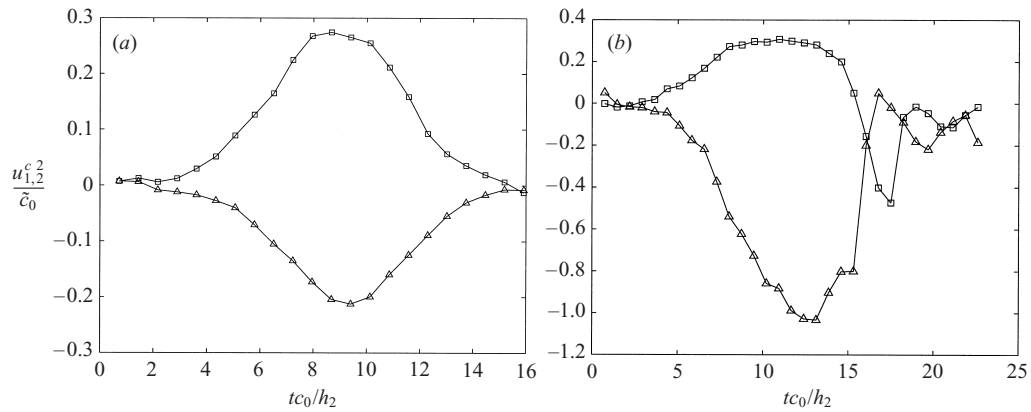FIGURE 9. Horizontal velocities above the ridge crest as a function of time, for $h_1/h_2 = 4.5$. Breaking is observed. $\square$, $\tilde{u}_2$; $\triangle$, $\tilde{u}_1$. (a) No breaking (*swl10*). (b) Breaking (*swl8*).
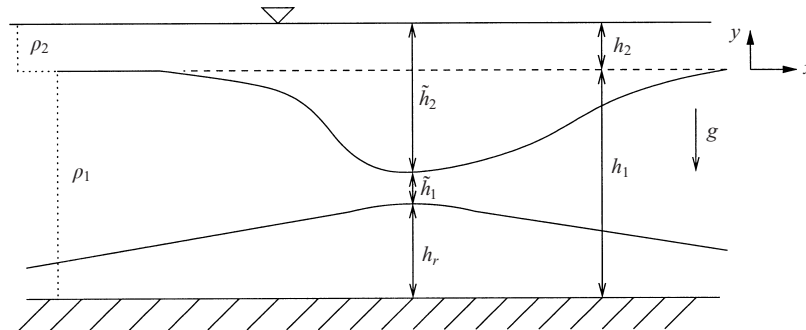

FIGURE 10. Definition sketch for the measurements at the second camera position.

velocity in the upper layer, $\tilde{u}_2(t = t_0) = \max(u_2^{c2}(t))$. Figure 9(a) shows an experiment where the interaction is characterized as weak. In this case, $|\tilde{u}_1|/\tilde{c}_0 \sim 0.21$. Turning to figure 9(b) where severe breaking is observed, the corresponding value is $|\tilde{u}_1|/\tilde{c}_0 \sim 1.16$.

It is noted that the measurement in figure 9(b) is not affected by the wave breaking until $t\tilde{c}_0/h_2 \sim 15$, implying that the breaking plays little part in the measurements of the minimum values of $\tilde{u}_1$. Other experiments (not shown here) verify that the largest absolute values are found before the effects of the breaking reach the measurement region. In the rest of the paper, the values of $|\tilde{u}_1|/\tilde{c}_0$ will always refer to measurements at camera 2.

The measured local velocities, $\tilde{u}_1$ and $\tilde{u}_2$, may now be used to estimate the excursion of the interface as a function of time. Figure 10 defines the local properties above the ridge crest. From continuity, $|\tilde{u}_2|\tilde{h}_2 \cong |\tilde{u}_1|\tilde{h}_1$ directly above the crest of the ridge, where $\tilde{h}_1 + \tilde{h}_2 = h_1 + h_2 - h_r$ (h_r the height of the ridge). The values of $\tilde{h}_1$ and $\tilde{h}_2$ can subsequently be used to define

$$\tilde{c}_0 = \sqrt{\frac{g'\tilde{h}_1\tilde{h}_2}{\tilde{h}_1 + \tilde{h}_2}}, \tag{4.4}$$

with $g' = g\Delta\rho/\rho$. The wave speed $\tilde{c}_0$ can be interpreted as the local (nonlinear) shallow-water speed at the top of the ridge.

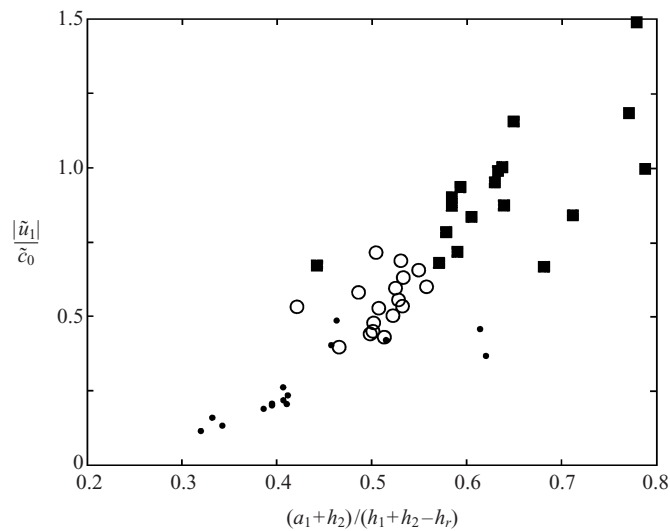Figure 11 shows a plot of the value of the local parameter, $|\tilde{u}_1|/\tilde{c}_0$, versus the

FIGURE 11. Non-dimensional amplitude of the incident wave versus horizontal, non-dimensional velocity above the ridge crest. Breaking is observed when the velocity in lower layer is greater than 70% of the value of the local linear long-wave speed, i.e. $|\tilde{u}_1|/\tilde{c}_0 > 0.70$. ●, Experiments where weak interaction is observed; ○, experiments where moderate interaction is observed; ■, experiments where the waves break as they pass the ridge.

amplitude of the incoming wave, $(a+h_2)/(h_1+h_2-h_r)$. With the previous classification of the interaction in mind, the plot in the figure can be used to classify the strength of the wave–ridge encounters as:

(i) For $|\tilde{u}_1|/\tilde{c}_0$ less than 0.4–0.5, the propagation of the solitary waves is not significantly altered by the presence of the ridge. Any attenuation of the wave amplitude is mainly ascribed to viscous effects.

(ii) For 0.4–$0.5 < |\tilde{u}_1|/\tilde{c}_0 < 0.7$, the effect on the wave due to the ridge causes steepening of the back of the wave and significant distortion above the ridge, though without breaking. A mild reduction of the wave amplitude and associated velocity magnitude downstream of the ridge is in evidence. Furthermore, separation effects take place at the ridge surface owing to the blockage-induced increased velocity within the lower layer.

(iii) For $|\tilde{u}_1|/\tilde{c}_0$ larger than about 0.7, the ridge has a significant impact on the wave, resulting in steepening and eventual breaking of the wave. Both the magnitude of the velocity and amplitude of the leading solitary wave are significantly reduced compared with the no-ridge case. For strong wave-breaking events, mixing and overturning take place. For all cases with $|\tilde{u}_1|/\tilde{c}_0 > 0.6$, vortices are observed to be generated at the up-slope side of the ridge as a wave propagates over it, as a result of flow separation.

The results above illustrate that wave breaking occurs when the particle velocity becomes comparable to the local nonlinear wave speed. The breaking occurs in the form of overturning of the wave. The overturning observed for $|\tilde{u}_1|/\tilde{c}_0 > 0.7$ (and not only for $|\tilde{u}_1|/\tilde{c}_0 > 1$) illustrates a transbreaking regime of the local process. The breaking observed here cannot be explained by shear instability (see §4.7).

4.6. *Breaking criterion expressed in terms of the incident wave*

It is tempting to relate the occurrence of breaking at the ridge, to the parameters of the incident wave and the ridge. As noted above, $|\tilde{u}_1|h_1 \cong |\tilde{u}_2|\tilde{h}_2$. It is furthermore
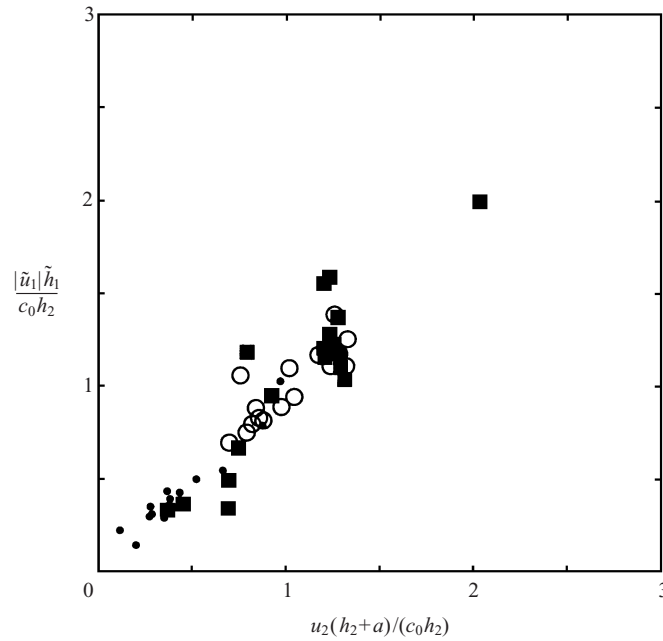
FIGURE 12. Volume flux of incoming wave, $u_2(h_2 + a)/(c_0 h_2)$, versus wave passing ridge, $|\tilde{u}_1|\tilde{h}_1/(c_0 h_2)$. Symbols as in figure 11.

noted that

$$|\tilde{u}_1|\tilde{h}_1 = |\tilde{u}_2|\tilde{h}_2 \sim u_2(a + h_2), \tag{4.5}$$

where u_2 and a denote the fluid velocity in the upper layer and the amplitude of the incident wave, respectively. This is confirmed by the plot in figure 12, roughly speaking. In the next step, the maximal thickness of the upper layer above the top of the ridge, $\tilde{h}_2$, is estimated by $\bar{h}_2 = a + h_2$. The corresponding thickness of the lower layer is $\bar{h}_1 = h_1 - h_r - a$. An estimate of $\tilde{c}_0$ is further given by $\bar{c}_0$ where $\bar{c}_0 = (g'\bar{h}_1\bar{h}_2/(h_1 + h_2 - h_r))^{1/2}$. Figure 13 plots $\tilde{c}_0$ versus $\bar{c}_0$, showing that the two quantities are almost equal for all measurements. It is then possible to estimate $\max |\tilde{u}_1|$ by $u_2(a + h_2)/\bar{h}_1$ and $\tilde{c}_0$ by $\bar{c}_0$. The breaking criterion $|\tilde{u}_1|/\tilde{c}_0 \gtrsim 0.7$ may then be indicated by the parameters of the incoming wave and the ridge by

$$\frac{u_2}{c_0} > f, \tag{4.6}$$

where u_2 denotes the maximal fluid velocity in the upper layer, owing to the incoming wave, c_0 is given by (2.1) and f by

$$f\left(\frac{a}{h_2}, \frac{h_r}{h_2}, \frac{h_2}{h_1}\right) = 0.7\frac{\bar{c}_0}{c_0}\frac{\bar{h}_1}{a + h_2}$$
$$= 0.7\frac{(1 + (h_2/h_1))^{1/2}}{(1 + (a/h_2))^{1/2}}\frac{((h_1/h_2) - (h_r/h_2) - (a/h_2))^{3/2}}{((h_1/h_2) - (h_r/h_2) + 1)^{1/2}}. \tag{4.7}$$

Values of u_2/c_0 may be taken from figure 3. Figure 14 supports the result that breaking occurs for u_2/fc_0 larger than 1. One of the cases with breaking stands out as an outlier, however. This is an experiment with $h_1 = 0.268$ m and $h_2 = 0.032$ m
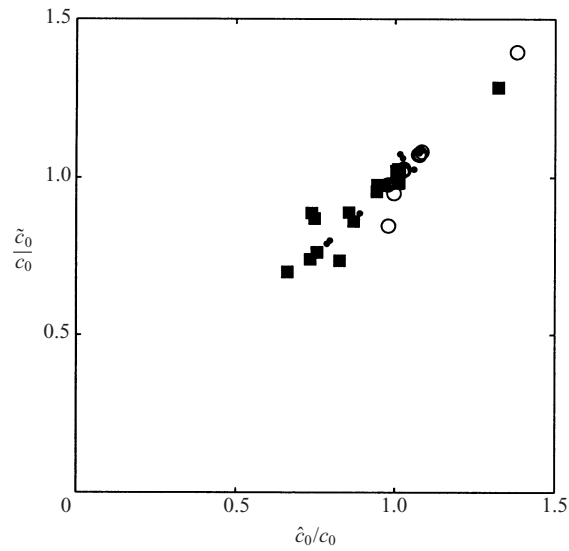
FIGURE 13. Non-dimensional, global c_0 plotted against non-dimensional local c_0. Symbols as in figure 11.
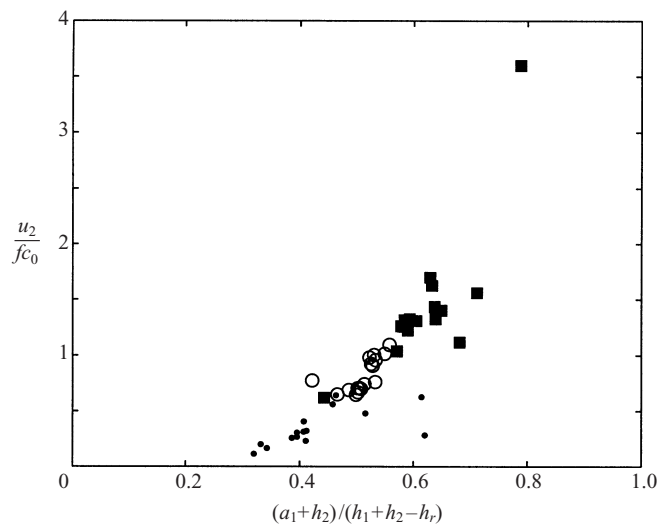

FIGURE 14. Non-dimensional horizontal velocities in the upper layer of the incoming wave *vs.* the non-dimensional amplitude. Symbols as in figure 11.

performed in the small wave tank where the relative interface thickness was of the same order of magnitude as the thickness of the upper layer. The velocity-field at the crest of the wave (not shown here) resembles the shape of that in a system with a linearly stratified upper layer and a lower thicker layer with constant density (see Grue *et al.* 2000). The case in figure 14 not fitting with (4.6)–(4.7) is thus ascribed to an uncertain determination of the incident wave.

The criterion (4.6)–(4.7) ties the occurrence of breaking to the properties of the incoming wave, the depth ratio between the fluid layers and the height of the ridge.

Experiment number	Tank	Observation	$\partial u/\partial y\|_{x=0}$ (s^{-1})	$\partial u/\partial y\|_{x=-3}$ (s^{-1})	$\|\tilde{u}_1\|/\tilde{c}_0$	$Ri\|_{x=0}$	$Ri\|_{x/h_2=-3}$
swl9	1	Moderate interaction	3.9	3.7	0.7	1.0	1.1
se45	2	Breaking (weak)	4.3	3.6	0.7	0.4	0.6
swl8	1	Breaking (strong)	4.4	4.0	1.2	0.8	0.9

TABLE 6. Table showing the Richardson number in three selected experiments.

4.7. *The role of shear instability*

Using the measured velocity fields, it is tempting to estimate the local Richardson number, $Ri = N^2/(\partial u/\partial y)^2$, as a function of time for a fixed position above the ridge crest. Here N is the Brunt–Väisälä frequency, and u the horizontal velocity above the ridge. This has been done for three selected experiments where $|\tilde{u}_1|/\tilde{c}_0$ ranges from 0.68 to 1.157. The maximal $\partial u/\partial y$ and minimal local Richardson numbers are shown in table 6. Ri is always significantly larger than 0.25, indicating that shear instability does not take place above the ridge crest in these experiments. An example can be seen in figure 6. In all three cases, a pycnocline thickness of 1.5 cm was used in the estimates of N.

It cannot be excluded that the shear instability contributes considerably to the breaking in the strong breaking cases. Indeed, it is observed that shear instability occurs in some of the experiments. This is true only in very strong breaking cases and then at an early stage of the wave–ridge encounter.

Additionally, in one of the experiments (see figure 7), shear instability was observed after the wave had broken in the form of a plunging jet. Billows were formed on an interface between the lower layer and the jet.

5. The transmitted wave

5.1. *The leading pulse*

A few experiments were conducted in the long wave tank with the purpose of measuring the transmitted wave over a relatively long period of time. The third camera was positioned between the ridge and the endwall of the channel, at 12.3 m, in the long tank, and at 4.9 m in the short tank, measured from the end of the tank where the waves were generated. Measurements of the motion from two selected experiments, where the interaction is characterized as moderate and strong, respectively, are presented. Data from other runs are available but not included here.

The transmitted waves were observed to consist of a leading solitary wavelike pulse travelling ahead of a train of smaller waves. In the cases where the interaction was characterized as weak (not shown here), the shape of the leading pulse closely resembled the numerical prediction of a solitary wave of permanent form and speed. In the case of moderate interaction, the overall shape of the initial pulse is broader than the incident solitary wave and the tail has not separated from the train that follows. In figure 15 (*swl9*, $|\tilde{u}_1|/\tilde{c}_0 = 0.72$), where the shape of the leading pulse is plotted and compared with a theoretical prediction for $a/h_2 = 0.53$, the leading part of the wave is seen to show very good agreement with a theoretical solitary wave profile. The tail of the wave, however, does not fit well with an ideal wave, which is due to the fact that the pulse has, at the time of measurement, not yet developed into a solitary wave. The amplitude of the leading pulse is observed to be about 30%
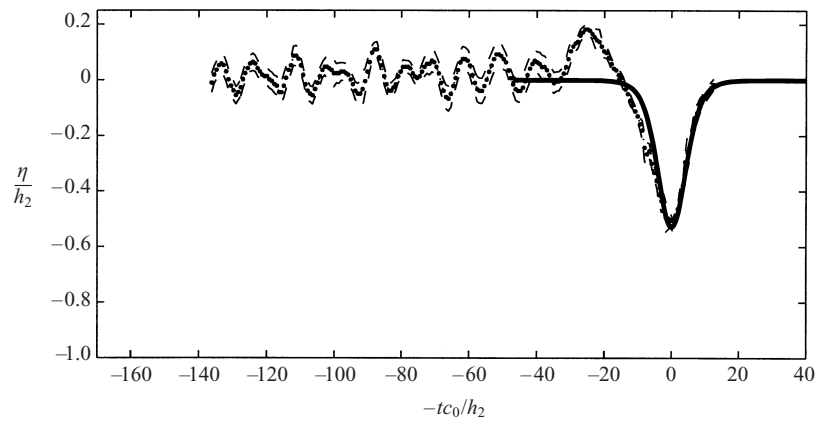
FIGURE 15. Interface, moderate interaction. Comparison of the leading pulse of the transmitted wave with a theoretical prediction for $a/h_2 = 0.53$. ——, Theory; ●, measurements; ——, estimated pycnocline thickness. Experiment *swl9*.
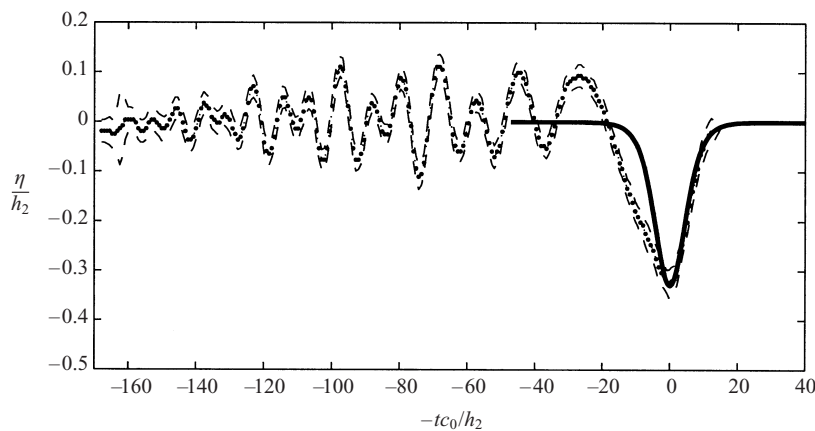

FIGURE 16. Interface, strong interaction. Comparison of the leading pulse of the transmitted wave with a theoretical prediction for $a/h_2 = 0.35$. Symbols are as for figure 15. Experiment *swl8*.

smaller than the amplitude of the incident wave. In the case with strong wave–ridge encounter, shown in figure 16, the front of the pulse exhibits good agreement with a theoretical profile for $a/h_2 = 0.35$, but the tail shows a significant deviation from this prediction. The amplitude of the leading pulse is observed to be about 41% smaller than the amplitude of the incident wave.

5.2. *The sequence of transient waves*

In all the experiments, a sequence of transient waves of small amplitude is generated downstream of the ridge, and these waves subsequently move following the leading pulse. Using the dispersion relation $\omega^2 = g'k[\coth(kh_2) + \coth(kh_1)]^{-1}$, an average wavenumber, k, may be calculated from the sequences by first estimating an average period in the wave sequence. In the experiments where the wave–ridge encounter was weak (results not shown), the sequence of waves travelling after the leading pulse consist of waves of fairly uniform amplitudes and frequencies. The wave sequence in figure 15 is taken from an experiment where the wave–ridge encounter is characterized as moderate. It has excursions varying from $\eta_{min}/h_2 \sim -0.06$ to $\eta_{max}/h_2 \sim 0.11$. In
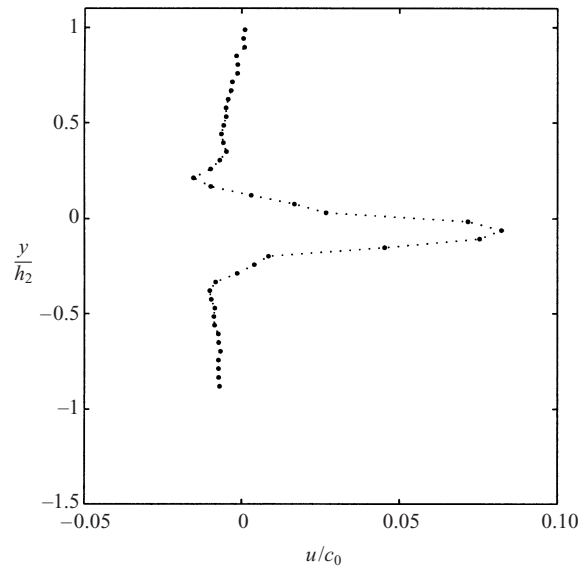
FIGURE 17. Horizontal velocity profile *vs.* non-dimensional depth. Internal wave of mode 2.

this case $\bar{\omega} = 2\pi/(10.6 h_2/c_0) = 0.823\,\mathrm{s}^{-1}$, $k = 7.6\,\mathrm{m}^{-1}$ and $\eta_{max} k = 0.0645$ are estimated. In another experiment (see figure 16), $|\tilde{u}_1|/\tilde{c}_0 \sim 1.16$ at the ridge, and strong breaking and mixing is observed. The waves in the sequence have maximal excursions between $\eta_{min}/h_2 \sim -0.11$ and $\eta_{max}/h_2 \sim 0.11$. The average frequency may be estimated as $\bar{\omega} = 2\pi/(9.4 h_2/c_0) = 0.917\,\mathrm{s}^{-1}$. The average wavenumber is $k = 8.82\,\mathrm{m}^{-1}$ and $\eta_{max} k = 0.0971$. The estimated $\bar{\omega}$ are much smaller than the Brunt–Väisälä frequency, which is about 4–$5\,\mathrm{s}^{-1}$, for the present experiments. Furthermore, it can be seen that the wavelengths are much shorter than the width of the ridge.

5.3. *Generation of internal waves of mode 2*

In the experiment depicted in figure 16, an internal wave of mode two has been generated at the ridge, with excursions into both layers, and is observed at $th_2/c_0 \sim 162$. This wave is generated as a result of breaking and is seen to propagate along the interface with excursions extending from $y/h_2 \sim 0.1$ to $y/h_2 \sim -0.2$, with $\Delta h/h_2 \sim 0.15$ and Δh being the thickness of the interface. Note that the measurements of interface motion do not capture this amplitude fully. Figure 17 shows the velocity profile measured, using PIV, through the crest of this mode-two wave. The maximum horizontal velocity measured is $u_{max}/c_0 = 0.082$, which is about 30% of the maximum velocity at the crest of the leading pulse.

5.4. *Wave-amplitude reduction*

A wave-amplitude reduction is caused by a combination of viscous effects and processes associated with the encounter between the wave and the bottom topography. A convenient measure of the integrated wave-amplitude reduction for the present geometries is provided by the wave-amplitude difference $(a^{\mathrm{cam1}} - a^{\mathrm{cam3}})$ between camera 1 and camera 3, normalized by the amplitude a^{cam1} at the first camera and scaled by the non-dimensional distance between the cameras. A non-dimensional
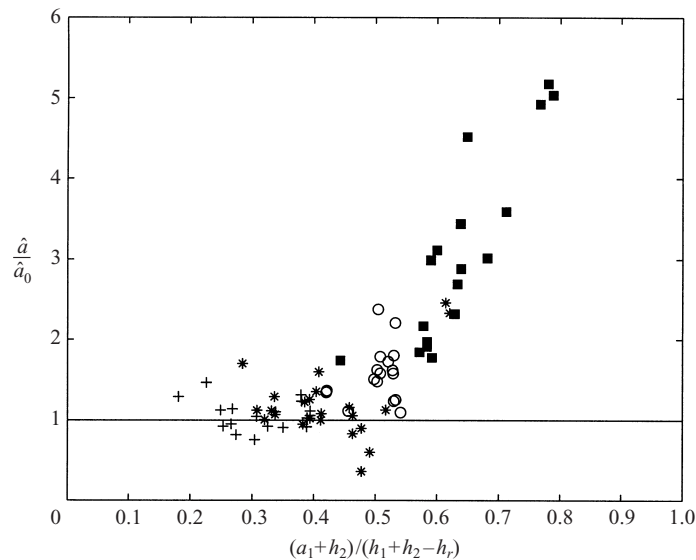
FIGURE 18. Amplitude reduction between the first and the third camera position. +, Measurements without a ridge present; *, measurements with a ridge present and where weak interaction is observed; ○, experiments with moderate interaction; ■, experiments where wave breaking was observed at the second camera position.

amplitude reduction or damping coefficient may thus be defined as

$$\hat{a} = \frac{(a^{\mathrm{cam1}} - a^{\mathrm{cam3}})/a^{\mathrm{cam1}}}{L_c/h_2}, \tag{5.1}$$

with L_c denoting the distance from the first to the third camera.

When there is no ridge present in the wave tank, this quantity gives a measure of the damping that the internal waves undergo during propagation. In this case, $\hat{a}$ is termed by $\hat{a}_0$. In the small tank, the associated damping coefficient $\hat{a}_0$, estimated from measurements at the first and third cameras are calculated to be 4.8% per metre, a value that agrees well with the results of Kao *et al.* (1985). This results in $\hat{a}_0 = 0.048h_2$. In the large wave channel the attenuation can be estimated using the results from Grue *et al.* (1999). Their data indicate an attenuation of about 1.3% per metre, giving $\hat{a}_0 = 0.013h_2$.

The properties of $\hat{a}$ may now be investigated. The results for all experiments herein are shown in figure 18. The data for $\hat{a}$ have been scaled with the appropriate $\hat{a}_0$ so that a value of 1 is equal to the damping that an internal wave undergoes when there is no ridge in the tank.

For the waves in the $|\tilde{u}_1|/\tilde{c}_0 < 0.4$–0.5 encounters, the ridge has no significant effect on the wave, and the reduction of the wave amplitude shows values that do not differ significantly from those without the ridge present. There is a sharp increase of the (leading) wave-amplitude reduction, however, when the blockage parameter $(a_1 + h_2)/(h_1 + h_2 - h_r)$ is larger than about 0.5–0.55. This coincides with the waves in the $0.5 < |\tilde{u}_1|/\tilde{c}_0 < 0.7$ regime where the ridge applies moderate modification to the wave. For values of $(a_1 + h_2)/(h_1 + h_2 - h_r)$ larger than about 0.55, the results show that the interaction with the ridge has significant impact on the amplitude reduction and that wave breaking occurs at the ridge. This also coincides with the experiments where breaking is observed and $|\tilde{u}_1|/\tilde{c}_0 > 0.7$.
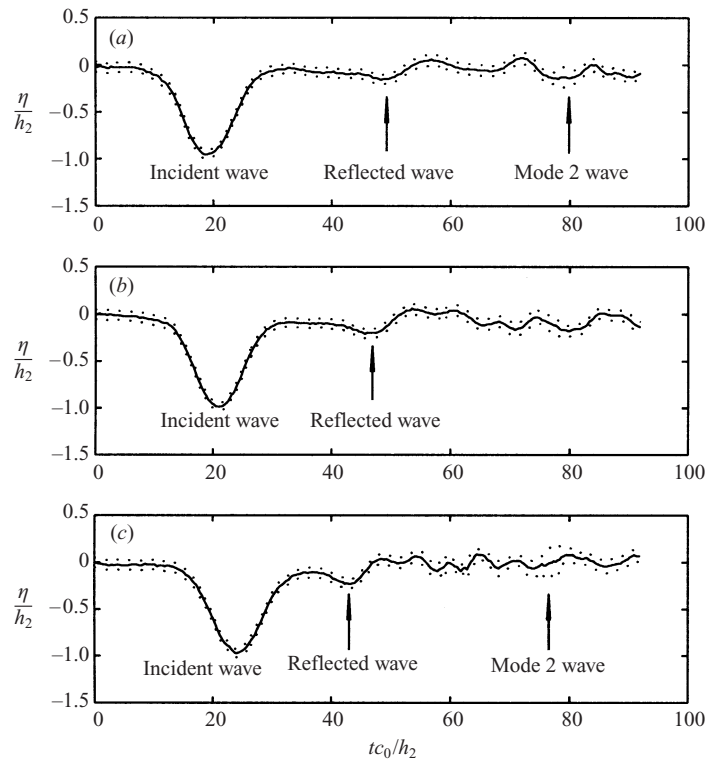
FIGURE 19. Reflected wave ($a/h_2 \sim 0.11$) for experiment *se49*, where strong breaking occurs. (*a*) The time trace at $x/h_2 = -2.1$. (*b*) $x/h_2 = 0$. (*c*) $x/h_2 = 3.5$. Solid arrows indicate position of reflected wave of mode 1, whereas dashed arrows indicate position of small mode 2 wave.

For all values of $\hat{a}/\hat{a}_0 > 2.5$, it is observed that the wave breaks at the ridge. This also implies that such a strong amplitude reduction of internal solitary waves can only be caused by breaking effects due to interaction with bottom topography. However, the authors are not aware of any *in situ* measurements of the amplitude damping and reduction of internal solitary waves for comparison with the above results.

6. Reflection, energy budgets and interaction at the ridge

6.1. *Reflected waves*

The wave–ridge encounter produces a reflected wave travelling from the ridge towards the first camera position. The data show evidence of solitary wave reflection for cases in which the topographic blockage is sufficiently great to effect significant distortions to the incoming wave. Figure 19 shows measurements at the first camera position for case *se49*. In this case, strong breaking was observed at the ridge. The vertical arrows in the figure indicate the position of the reflected waves. The solid arrows indicate the position of a mode 1 wave of amplitude $a/h_2 \sim 0.11$. A wave of mode 2 is observed propagating from the ridge back past the first camera position. In the cases with strong interaction, the amplitude of the reflected waves are estimated to be between 10% and 15% of that of the incident waves. This implies that the total energy in the reflected wave is about 1–2% of that of the incident wave. For cases where the

Experiment number	Energy in incident wave cam1 10% reduced	Energy in transmitted leading wave $\dfrac{T+V}{\rho_1 g' h_2^3}$	Energy in wave train $\dfrac{T+V}{\rho_1 g' h_2^3}$	Loss %
swl7	0.92	0.66	0.03	25%
swl9	8.06	4.52	0.3	40%
swl8	4.41	2.03	0.56	41%

TABLE 7. Energy.

topographic effect was weak (low ridge, small-amplitude waves) no reflected waves were detected.

Diebels *et al.* (1994) have studied transmission and reflection of internal solitary wave at a topography. They considered two cases, the first in which a thick layer was above a thin layer, with topography in the latter. In this case a pronounced reflection wave was measured when the height of the topography exceeded the thickness of the thin layer. The incoming waves were solitary waves of elevation. In the second case, discussed in their §4, they used a thin layer above a thick layer. Incoming solitary waves of depression were incident upon a bottom topography in the lower layer. Only very small reflection waves were observed (their figures 11–13). The experimental results in Diebels *et al.* (1994) and Wessels & Hutter (1996) correspond. The observations presented herein, of reflection waves of relatively small amplitude, for a thin layer above a thick, and with the topography in the thicker (lower) layer, correspond to the observations in these mentioned papers.

6.2. *Energy budgets*

It may be of interest to consider the energy budget for a few selected experiments performed in the long wave tank. The kinetic and potential energy in the solitons are computed with the fully nonlinear method (Grue *et al.* 1999; Rusås 2001), given the amplitude of the wave. The energy of the incoming soliton is compared with that of the transmitted leading pulse plus transient tail. The reduction of the amplitude owing to dissipation, of the incident wave, is accounted for (1.3% per metre). The mechanical energy in the wave sequence following the leading pulse is estimated by $(T+V) \cong 2V = 1/2\rho_1 g' a^2 \lambda n$, where a denotes the amplitude, $\lambda = 2\pi/k$ and n is the number of waves in the sequence. The results are shown in table 7. The column on the right-hand side of the table indicates a loss due to the encounter between the incident wave and the ridge.

6.3. *Trapped waves over the ridge*

No evidence of a trapped wave was detected for any of the cases investigated. For the cases of strong wave–ridge encounter, the motion above the ridge is dominated by wave breaking. The presence of any trapped wave in these circumstances is therefore likely to be hidden by the more dramatic manifestations of the above breaking (overturning and mixing, followed by the local formation of laterally intruding flows).

6.4. *Resonance over the ridge*

When the width of the ridge matches that of the incident wave, one might be inclined to expect a resonance over the ridge. To investigate this, two laboratory

experiments (not shown here) were carried out for cases (i) in which the topographic blockage was sufficiently weak for breaking not to occur, according to the ridge-height breaking criterion, but for which (ii) the width matched/did not match, respectively, the wavelength of the solitary wave. No significant differences were detected in the change in the amplitude of the wave over the topographically tuned and non-tuned cases, respectively. In addition, no evidence of significant resonant increase or decrease of wave amplitude as a result of the encounter was measured for the topographically tuned ridge, as compared with the reference, non-tuned ridge under otherwise identical conditions.

7. Concluding remarks

Focus in this paper has been internal solitary waves of depression encountering a submerged ridge. The solitary waves were generated in a two-layer system with a thin upper layer and a relatively thicker lower fluid layer, each layer with a constant density. The wave amplitudes of the generated solitary waves were in the range 0.2–1.9 times the depth of the upper layer, and the ratio between the lower and the upper layer was in the range 3.0–8.5. Experiments were carried out in two different wave tanks, one small and one larger. A total of four different ridges were used, with shapes as indicated in figure 1 and table 1. The ridge slope was varied from 0.1 to 0.33 and the maximum relative ridge height was two-thirds of the thicker fluid layer and three times the thinner one. The ridge used in the long wave tank had the smallest slope.

Experiments were performed for (i) strong interaction between the wave and the ridge, (ii) moderate interaction, (iii) weak interaction and (iv) no interaction (no ridge present). Most attention was paid to the case of a strong interaction where the incoming wave broke at the ridge. Breaking happened in the form of either spilling or overturning in the tail of the wave. In the experiments with the wide ridge, a wave of elevation was formed in the tail of the wave. Breaking was observed in the front and also in the tail of the wave of elevation, the former taking place at an earlier time than the latter. Such a breaking was not observed in the experiments with the narrow ridges. In these cases a strong forward plunging breaker was observed.

In all the cases with breaking, vortices were shed on the upslope side of the ridge. Tracer particles were transported vertically, from the top of the ridge, and relatively high up into the fluid. A maximum level was the middle of the upper fluid layer. The buoyancy anomaly became, in the breaking cases, up to about 25% of a theoretical maximum, where all mechanical energy is lost in the breaking process.

Details of the local wave-induced flow at the ridge have been quantified and visualized. A breaking condition was identified. Breaking was found to take place when the fluid velocity in the lower layer exceeded 0.7 of a local nonlinear wave speed at the top of the ridge (defined in equation (4.4)), i.e. somewhat less than critical flows (see equation (4.5)). The occurrence of breaking was also determined in terms of the amplitude of the incoming wave, the layer thickness ratio and the relative height of the ridge, see equation (4.7). This means that wave breaking can be determined from the input parameters of the experiment.

The transmitted waves were composed by a leading pulse and a dispersive wave-train. The transmitted leading pulse was always identified as a solitary wave. It could be significantly smaller than the incoming wave only when breaking took place at the ridge (figure 18). Waves that did not break at the ridge were not reduced in amplitude, practically speaking. The train of dispersive waves were all with small wave slope (linear) and had periods significantly shorter than the leading pulse.

Waves of mode 2 were also generated in runs with strong breaking at the ridge, propagating along the pycnocline. An example is visualized in figure 17. The maximum horizontal fluid velocity induced by the mode 2 wave was found to be up to 30% of the maximum fluid velocity induced by the leading transmitted pulse.

REFERENCES

APEL, J. R., HOLBROOK, J. R., LIU, A. K. & TSAI, J. J. 1985 The Sulu Sea internal soliton experiment. *J. Phys. Oceanogr.* **15**, 1625–1651.

BENJAMIN, T. B. 1966 Internal waves of finite amplitude and permanent form. *J. Fluid Mech.* **25**, 241–270.

COOKER, M. J., PEREGRINE, D. H., VIDAL, C. & DOLD, J. W. 1990 The interaction between a solitary wave and a submerged semicircular cylinder. *J. Fluid Mech.* **215**, 1–22.

DALZIEL, S. B. 1992 Decay of rotating turbulence: some particle tracking experiments. *Appl. Sci. Res.* **49**, 217–244.

DALZIEL, S. B. 1993 Rayleigh–Taylor instability: experiments with image analysis. *Dyn. Atmos. Oceans* **20**, 127–153.

DE SILVA, I. P. D., IMBERGER, J. & IVEY, G. N. 1997 Localized mixing due to a breaking internal wave ray at a sloping bed. *J. Fluid Mech.* **350**, 159–177.

DIEBELS, S., SCHUSTER, B. & HUTTER, K. 1994 Nonlinear internal waves over variable topography. *Geophys. Astrophys. Fluid Dyn.* **76**, 165–190.

DJORDJEVIC, V. D. & REDEKOPP, L. G. 1978 The fission and disintegration of internal waves moving over two-dimensional topography. *J. Phys Oceanogr.* **8**, 1016–1090.

GRIMSHAW, R., PELINOVSKY, E. & TALIPOVA, T. 1998 Solitary wave transformation due to a change in polarity. *Stud. Appl. Maths* **101**, 357.

GRUE, J., FRIIS, H. A., RUSÅS, P.-O. & PALM, E. 1997 A method for computing unsteady fully nonlinear interfacial waves. *J. Fluid Mech.* **351**, 223–252.

GRUE, J., JENSEN, A., RUSÅS, P.-O. & SVEEN, J. 1999 Properties of large amplitude internal waves. *J. Fluid Mech.* **380**, 257–278.

GRUE, J., JENSEN, A., RUSÅS, P.-O. & SVEEN, J. 2000 Breaking and broadening of internal solitary waves. *J. Fluid Mech.* **413**, 181–217.

GRUE, J. & OSTROVSKY, L. A. 2001 Strongly nonlinear internal solitions – analytical models and fully nonlinear computaitons. Submitted.

HEAD, M. J. 1983 The use of four-electrode conductivity probes for high-resolution measurement of turbulent density or temperature variation in salt-stratified water flows. PhD thesis, University of California, San Diego, USA.

HELFRICH, K. R. 1992 Internal solitary wave breaking and run-up on a uniform slope. *J. Fluid Mech.* **243**, 133–154.

HELFRICH, K., MELVILLE, W. K. & MILES, J. 1984 On interfacial solitary waves over slowly varying topography. *J. Fluid Mech.* **149**, 305–317 (and Corrigendum, **155** 1985, 535).

HOUGH, G. & MORAN, J. 1969 Froude number effects on two-dimensional hydrofoils. *J. Ship Res.* **13**(1).

HUTHNANCE, J. M. 1989 Internal tides and waves near the continental shelf edge. *Geophys. Astrophys. Fluid Dyn.* **48**, 81–106.

JOHNSON, R. S. 1973 On an asymptotic solution of the Korteweg–de Vries equation with slowly varying coefficients. *J. Fluid Mech.* **60**, 813–824.

KABBAJ, A. 1985 Contribution à l'étude du passage des ondes de gravité sur le talus continental et à la gènèration des ondes internes. PhD thesis, Ètat, Univ. Sci. Mèd. Grenoble.

KABBAJ, A. & ZHANG, X. 1988 Passage d'une onde interne solitaire sur un seuil d'après le modèles analytiques de Djordjevic–Redekoppe et de Kabbaj. *Oceanologica Acta* **11**, 315.

Kao, T. W., Pan, F.-S. & Renouard, D. 1985 Internal solitons on the pycnocline: generation, propagation, and shoaling and breaking over a slope. *J. Fluid Mech.* **159**, 19–53.

Keulegan, G. H. 1953 Characteristics of internal solitary waves. *J. Res. Natl Bur. Stand.* **51**, 133–140.

Knickerbocker, C. J. & Newell, A. C. 1980 Internal solitary waves near a turning point. *Phys. Lett.* A **75**, 326.

Koop, C. G. & Butler, G. 1981 An investigation of internal solitary waves in a two-fluid system. *J. Fluid Mech.* **112**, 225–251.

Long, R. R. 1956 Solitary waves in one- and two-fluid systems. *Tellus* **8**, 460–471.

Malomed, B. & Shrira, V. 1991 Soliton caustics. *Physica* D **53**, 1.

Michallet, H. & Barthelémy, E. 1998 Experimental study of interfacial solitary waves. *J. Fluid Mech.* **366**, 159–177.

Michallet, H. & Ivey, G. N. 1999 Experiments on mixing due to internal solitary waves breaking on uniform slopes. *J. Geophys. Res.* **104**, 13 467–13 477.

Ono, H. 1972 Wave propagation in an inhomogeneous and harmonic lattice. *J. Phys. Soc. Japan* **32**, 332–336.

Osborne, A. R. & Burch, T. L. 1980 Internal solitons in the Andaman Sea. *Science* **208**, 451–460.

Osborne, A. R., Burch, T. L. & Scarlet, R. I. 1978 The influence of internal waves on deep water drilling. *J. Petrol. Technol.* **30**, 1497–1504.

Ostrovsky, L. A. & Stepanyants, Y. A. 1989 Do internal solitons exist in the ocean? *Rev. Geophys.* **27**, 293–310.

Raffel, M., Willert, C. E. & Kompenhans, J. 1998 *Particle Image Velocimetry, A Practical Guide*, 1st Edn. Springer.

Renouard, D. P., Seabra Santros, F. J. & Zhang, X. 1987 Étude expérimentale du passage d'une onde solitaire au-dessus d'un seuil. *Oceanologica Acta* **10**, 256.

Rusås, P.-O. 2001 Method for computing fully nonlinear interfacial two-layer waves. http://bukharin.hiof.no/~por/internalwaves.

Sandstrom, H. & Elliott, J. A. 1984 Internal tide and solitons on the Scotian shelf: a nutrient pump at work. *J. Geophys. Res.* **89**, 6415–6426.

Segur, H. & Hammack, J.-L. 1982 Soliton models of long internal waves. *J. Fluid Mech.* **118**, 285–304.

Sveen, J. K. 1998 An introduction to MatPIV v1.4 – the particle image velocimetry toolbox for Matlab. http://www.math.uio.no/~jks/matpiv.

Walree, F. V. 1999 Computational methods for hydrofoil craft in steady and unsteady flow. PhD thesis, Technical University Delft.

Wessels, F. & Hutter, K. 1996 Interaction of internal waves with a topographic sill in a two-layer fluid. *J. Phys. Oceanogr.* **26**, 5–20.

Westerweel, J., Dabiri, D. & Gharib, M. 1997 The effect of a discrete window offset on the accuracy of cross-correlation analysis of digital PIV recordings. *Exps. Fluids* **23**, 20–28.

Willert, C. E. & Gharib, M. 1991 Digital particle image velocimetry. *Exps. Fluids* **10**, 181–193.